



HAL
open science

Greener and more mechanically robust 3D acrylate composites with added tannin

Pauline Blyweert, Vincent Nicolas, Vanessa Fierro, Alain Celzard

► **To cite this version:**

Pauline Blyweert, Vincent Nicolas, Vanessa Fierro, Alain Celzard. Greener and more mechanically robust 3D acrylate composites with added tannin. *Industrial Crops and Products*, 2023, 203, pp.117179. 10.1016/j.indcrop.2023.117179 . hal-04274072

HAL Id: hal-04274072

<https://hal.science/hal-04274072>

Submitted on 7 Nov 2023

HAL is a multi-disciplinary open access archive for the deposit and dissemination of scientific research documents, whether they are published or not. The documents may come from teaching and research institutions in France or abroad, or from public or private research centers.

L'archive ouverte pluridisciplinaire **HAL**, est destinée au dépôt et à la diffusion de documents scientifiques de niveau recherche, publiés ou non, émanant des établissements d'enseignement et de recherche français ou étrangers, des laboratoires publics ou privés.



Distributed under a Creative Commons Attribution - NonCommercial - NoDerivatives 4.0 International License

Greener and more mechanically robust 3D acrylate composites with added tannin

Pauline Blyweert^a, Vincent Nicolas^a, Vanessa Fierro^a, Alain Celzard^{a,b*}

^a Université de Lorraine, CNRS, IJL, F-88000, Epinal, France

^b Institut Universitaire de France (IUF)

Keywords

3D printing; Biocomposite; Mechanical properties; Particle-reinforcement

Abstract

Greener and more mechanically robust 3D-printed structures were obtained by adding tannin to acrylate resin. Mimosa tannin particles (5-25wt.%) were incorporated into an acrylate resin formulated and 3D-printed to fabricate tannin-reinforced composites using stereolithography. FTIR spectroscopy and printing parameters highlighted the photoblocking behavior of the tannin particles by adsorption in the UV range and a reddening phenomenon characteristic of phenolic compounds. Tannin-containing samples showed a low penetration depth (from 322 to 127 μ m), thus improving the resolution control in the resin tank. The glass transition temperature decreased with the incorporation of stiff tannin microparticle, evidencing change in relaxation time, while mechanical properties improved with increasing tannin content. For instance, the inclusion of 10 wt.% tannin improved tensile strength, ductility, and Young's modulus by 110, 80, and 32%, respectively. The high resolution and improved mechanical performance demonstrate the promising use of tannin as a bio-based ingredient to produce accurate and reinforced structures.

24 **1. Introduction**

25 Additive manufacturing, also known as rapid prototyping or 3D printing, enables on-
26 demand production of complex architectures from digital model designs (ISO/ASTM, 2016;
27 Thakar et al., 2022). Among the many 3D printing technologies, laser stereolithography (SLA)
28 is a versatile and accurate method for printing complex parts with high resolution (as low as
29 10 μm), fast printing time, and simple post-processing requirements (Cingesar et al., 2022;
30 Oliaei and Behzad, 2019; Pagac et al., 2021; Zhao et al., 2020). Evolving rapidly since the
31 1980s, stereolithography has become an essential tool for research and industry, be it
32 aerospace, automotive, healthcare or even art (Quan et al., 2020; Tan et al., 2022; Zhang et al.,
33 2020, p. 3). Consequently, this leads to an increased demand to develop new materials and
34 continuously improve their properties and accuracy to meet the needs of various applications.

35 Commercial photocurable resins used in SLA are usually based on (meth)acrylate polymer
36 formulations. Nevertheless, these particularly brittle thermosets have sometimes poor
37 mechanical properties (Anastasio et al., 2019; Manapat et al., 2017a). Research has therefore
38 turned to the development of polymer composites in which the incorporation of a rigid filler
39 (carbon fiber, glass fiber, silica, or graphene oxide, to name a few) improves the properties of
40 the matrix (Blyweert et al., 2021; Manapat et al., 2017a; Palaganas et al., 2019; Wu et al.,
41 2020).

42 In the context of climate change and the search for more sustainable approaches,
43 significant efforts have been devoted to the development of 3D printing materials containing
44 abundant renewable resources or agro-residues such as chitin, cellulose, vegetable oils, or
45 lignin (Feng et al., 2022; Kumar et al., 2012; Maalihan et al., 2020, 2022; Romero-Ocaña et
46 al., 2022; Sutton et al., 2018; S. Zhang et al., 2019; Zhang et al., 2021; Zhu et al., 2022). For
47 example, Maalihan *et al.* (Maalihan et al., 2020) showed that chitin nanowhiskers improved
48 the tensile strength of SLA-printed composites, and that their functionalization could

49 strengthen and toughen the printed items at the same time (Maalihan et al., 2022). Sutton *et al.*
50 (Sutton et al., 2018) and Zhang *et al.* (S. Zhang et al., 2019) studied the effectiveness of lignin
51 reinforcement of commercial photoreactive resins and found that the inclusion of a few
52 percent lignin increased tensile and flexural strength while improving printing accuracy.

53 Among the many bio-based fillers available, condensed tannin has received much less
54 attention than its counterparts as a reinforcing filler. Generally used as raw material for the
55 preparation of gels, foams, adhesives, and composite materials (Braghiroli et al., 2019;
56 Celzard and Fierro, 2020; V. Dhawale et al., 2022), Mimosa tannin, a low-cost natural and
57 abundant polyphenolic resource, has more recently gained attention as a promising additive
58 for the 3D printing of carbon parts (Blyweert et al., 2023, 2022b, 2022a). However, the
59 literature on the use of condensed tannin as a filler material has mainly been limited to certain
60 thermoplastic composites prepared by extrusion (Ambroggi et al., 2011; Anwer et al., 2015;
61 Liao et al., 2020), giving a first glimpse of the fillers' potential for additive manufacturing.
62 Herein, we propose the first study of stereolithographically-printed acrylate-tannin composite
63 parts, ensuring high resolution and improved mechanical properties. Samples printed with
64 blends of tannin and acrylate resin were prepared, and it was determined that even high
65 loading (up to 25 wt.%) of tannin could significantly improve the mechanical performance of
66 the fabricated parts. This research not only expands the use of mimosa tannin in the 3D
67 printing field, but also proves that tannin can act as a multitask filler for SLA resins.

68 **2. Experimental section**

69 *2.1. Materials*

70 Hexanediol diacrylate (HDDA, SR238), pentaerythritol tetraacrylate (PETA, SR295), and
71 acrylate oligomer (CN154 CG) were supplied by Sartomer (Arkema Group, France).
72 Bis(2,4,6-trimethylbenzoyl)phenylphosphine oxide (BAPO) was purchased from Lambson

73 (Arkema Group, England). Mimosa (*Acacia Mearnsii*) tannin extract was kindly provided by
74 SilvaChimica (St Michele Mondovi, Italy) and used as a bio-based precursor. All products
75 were used as received.

76 *2.2. Preparation and 3D printing of tannin-acrylate composites*

77 Tannin-acrylate composites were prepared by adding varying amounts of tannin to an
78 acrylate-based resin (containing HDDA, PETA, CN154 and BAPO, see Table S1) using a tip
79 sonicator for 10 min to ensure homogeneous dispersion in the resin. The relative proportions
80 between the different acrylate resin ingredients being constant, the samples were therefore
81 named T-x accordingly, where x = 0, 5, 10, 15, 20 or 25 wt.% is the mass fraction of tannin in
82 the final mixture.

83 The samples were then printed as 30- μm slices using a DWS 28J (DWS, Italy), a high-
84 resolution (17 μm horizontally, 10 μm vertically) SLA 3D printer operating with a 405 nm
85 laser. The printed samples were then rinsed in isopropanol and post-cured in a UV oven (same
86 wavelength as the laser of the 3D printer) for 20 min at room temperature.

87 *2.3. Characterisation techniques*

88 *2.3.1. Viscosity, polymerization kinetics and printability*

89 A Brookfield DVII+ PRO viscometer with cone-plate geometry (spindle CPE-51, gap
90 0.013 mm) was used to measure the viscosity of the resins at room temperature.

91 FTIR spectra were obtained using a Frontier Spotlight 400 spectrometer (Perkin Elmer,
92 UK) in ATR mode in the 4000-600 cm^{-1} wavenumber range. The photopolymerization
93 reactivities of the tannin-acrylate resins were determined by monitoring of the acrylate
94 characteristics peak (C=C stretching, at 1635 cm^{-1}) after several irradiation times in a UV
95 oven at 405 nm (Lee et al., 2003). Four cumulative scans with a resolution of 1 cm^{-1} were
96 collected. Equation (1) was used to determine the C=C conversion (α).

$$\alpha (\%) = \frac{A_0 - A_t}{A_0} \times 100 \quad (1)$$

97 where A_0 is the absorbance of the system at the characteristic peak (1635 cm^{-1}) before
 98 irradiation and A_t is the corresponding absorbance at a given irradiation time t . The derivative
 99 of α with respect to time allows the polymerization rate ($d\alpha/dt$) to be obtained.

100 The working curve model for laser stereolithography (SLA), *i.e.*, the so-called Jacobs
 101 model (Jacobs, 1992), which is fundamental for determining the operating parameters, is
 102 described by equation (2), derived from the Beer-Lambert law (Lee et al., 2001):

$$C_d = D_p \ln \left(\frac{E_{max}}{E_c} \right) \quad (2)$$

103 where C_d (μm) is the curing depth of a single laser-cured layer, D_p (μm) is the depth of
 104 penetration, *i.e.*, the depth at which the irradiance I ($\text{W}\cdot\text{m}^{-2}$) is about 37% (*i.e.*, $1/e$, with $\ln(e)$
 105 $= 1$) of the irradiance I_0 at the resin surface, E_c ($\text{mJ}\cdot\text{cm}^{-2}$) is the exposure required for the resin
 106 to reach its gel point, and E_{max} ($\text{mJ}\cdot\text{cm}^{-2}$) is the maximum exposure at the resin surface. D_p
 107 and E_c are the characteristic parameters for a given resin in a 3D printer and were estimated
 108 for the different tannin contents by varying the exposure of the resin and measuring the
 109 resulting curing depth.

110 The maximum exposure is determined from equation (3): (Jacobs, 1992)

$$E_{max} = \sqrt{\frac{2}{\pi}} \frac{P_L}{W_0 \cdot V_s} \quad (3)$$

111 where P_L (W) is the laser power, W_0 (m) is the beam width and V_s ($\text{m}\cdot\text{s}^{-1}$) is the scan speed. P_L
 112 and W_0 for the printer used in this work were 0.032 W and 17 μm , respectively. The different
 113 exposures were obtained at varying speeds between 0.25 and 2 $\text{m}\cdot\text{s}^{-1}$.

114 2.3.2. *Thermal stability and physical properties*

115 Thermogravimetric measurements of the photocured resins were carried out under argon
116 atmosphere using a Netzsch STA 449 F3 Jupiter thermobalance with a heating rate of
117 $10\text{ }^{\circ}\text{C}\cdot\text{min}^{-1}$ from room temperature to $800\text{ }^{\circ}\text{C}$. A Netzsch 402 F1 Hyperion®
118 thermomechanical analyzer (TMA) was used in dynamic mode (DTMA) to evaluate the
119 viscoelastic properties of the cured resins. A three-point bending geometry with a frequency
120 of 0.1 Hz , an amplitude of 30 mN and a constant offset force of 50 mN were used. Samples
121 were printed with appropriate dimensions ($25\text{ mm} \times 5\text{ mm} \times 1\text{ mm}$) and were tested following
122 McAninch *et al.* (McAninch et al., 2015) with a temperature ramp of $10\text{ }^{\circ}\text{C}\cdot\text{min}^{-1}$ from 20 to
123 $200\text{ }^{\circ}\text{C}$.

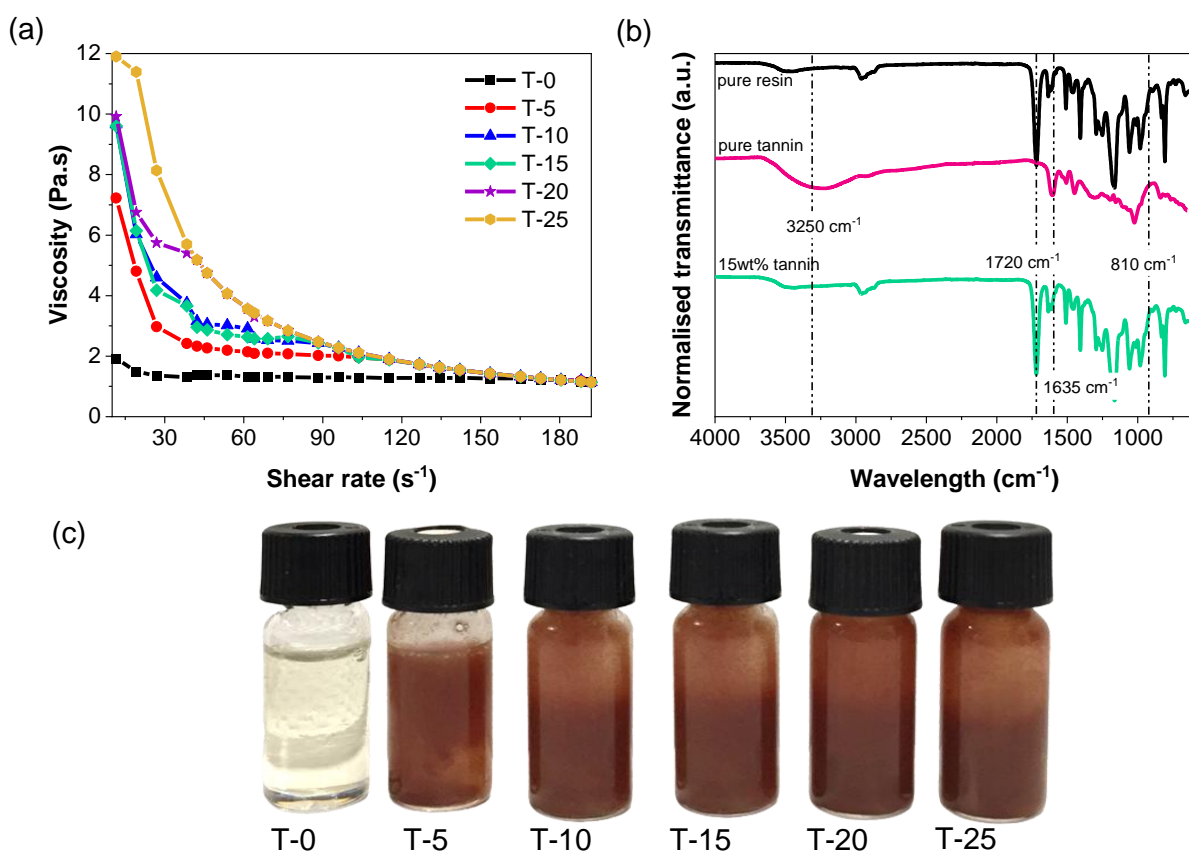
124 Tensile tests were carried out on printed dogbone specimens (ISO 527-2, 5B sample, 35
125 mm length and 2 mm thickness) using an Instron universal testing machine with a 2 kN load
126 cell and a tensile speed of $5\text{ mm}\cdot\text{min}^{-1}$ in accordance with ASTM ISO 527. The samples were
127 printed such that the printed layers were parallel to the direction of the tensile stress.

128 **3. Results and discussion**

129 *3.1. Characterisation of tannin-acrylate resins*

130 Viscosity is a crucial parameter for 3D printing with a stereolithography machine. In
131 general, low viscosities are desired to allow for fast and fluent recoating of the liquid resin
132 between the last printed layer and the surface of the resin tank; thus, the viscosity of
133 photocurable resins is generally preferred below $3\text{ Pa}\cdot\text{s}$ (Weng et al., 2016; Zakeri et al.,
134 2020). The viscosity of uncured acrylate-tannin resins was determined as a function of shear
135 rate (**Figure 1a**). Newtonian behavior was observed for the unfilled resin (T-0), while shear-
136 thinning behavior at low shear rate was obtained for the resin containing tannin. This behavior,
137 typical of particle-loaded suspension (see Figure 1c), is related to particle-particle and
138 particle-fluid interactions under shear (Lobry et al., 2019; Mangesana et al., 2008; Mewis,

139 1980). The viscosity at low shear increased from 1.9 to 11.9 Pa·s, with tannin content
140 increasing from 0 to 25 wt.%. Nonetheless, at a high shear rate of 100 s^{-1} (commonly achieved
141 during the recoating step), the viscosity of the different resins tended towards 1.3 Pa·s, thus
142 demonstrating adequate viscosity for stereolithography printing. It is important to note that
143 above a 30 wt.% loading, the viscosity of the formulation increases significantly until it forms
144 a paste, making the resin unprintable.



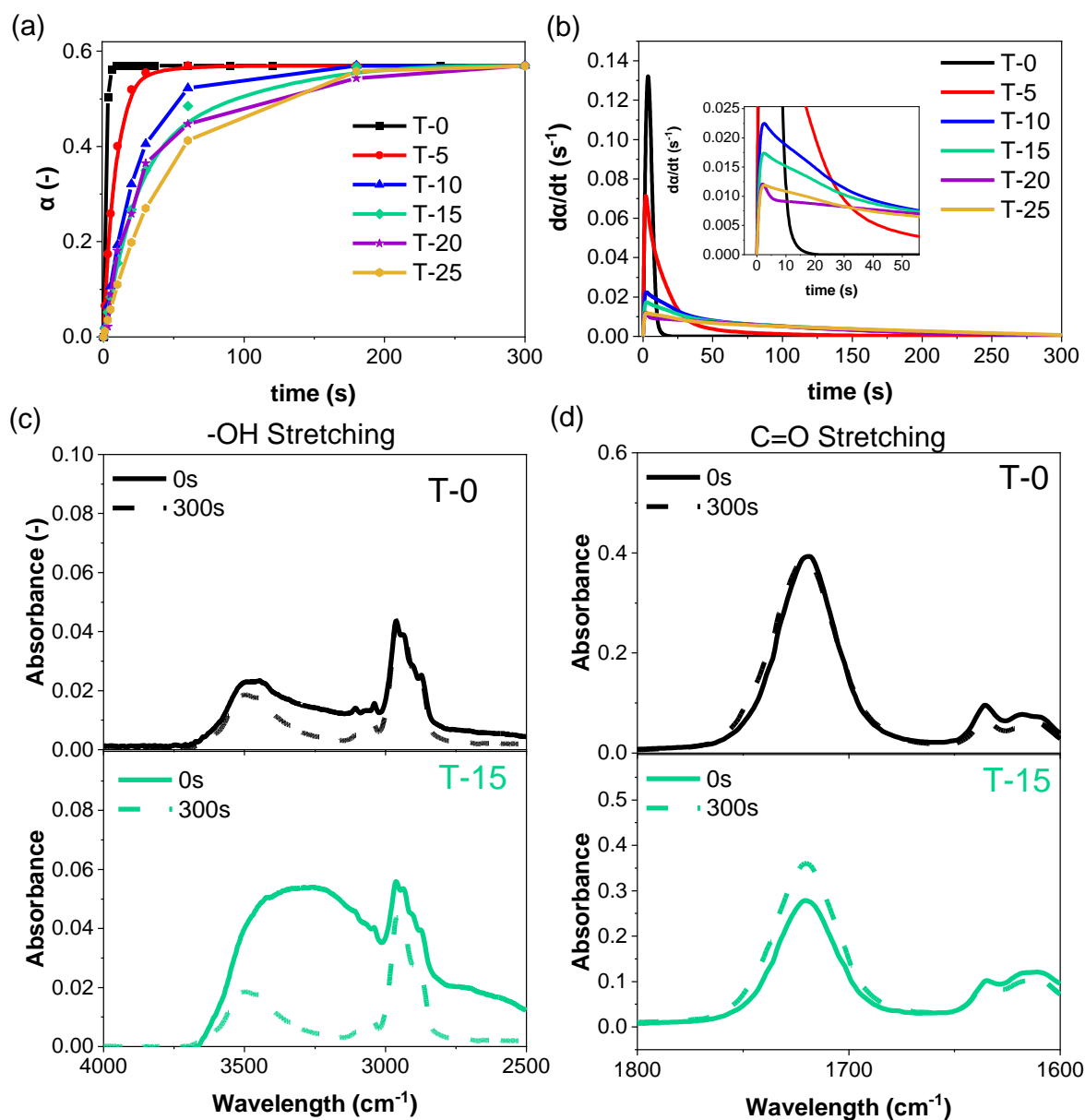
145
146 **Figure 1.** (a) Viscosity versus shear rate of acrylate resin containing different weight
147 fractions of tannin (from 0 wt.% for T-0 to 25wt.% for T-25); (b) FTIR spectra of uncured
148 acrylate resin, acrylate-tannin composite containing 15 wt.% of filler and pure Mimosa tannin
149 powder (c) tannin-based acrylate resin with different tannin contents.

150 FTIR spectroscopy was conducted to investigate the chemical structure of the composites.
151 The spectra of tannin powder, neat acrylate resin, and their nanocomposites with 15 wt.%

152 filler are presented in **Figure 1b**. The spectrum of the acrylate resin reveals the characteristics
153 bands of a typical photocurable (meth)acrylate formulation designed for SLA: 2920 cm^{-1} (C-
154 H asymmetric stretching), 1720 cm^{-1} (C=O stretching in ester groups), 1635 cm^{-1} (ethylenic
155 C=C stretching), 1180 cm^{-1} (C-O-C stretching in ester groups) and 810 cm^{-1} (ethylenic C=C
156 bending) (Manapat et al., 2017b; X. Zhang et al., 2019). Peaks related to -OH stretching in
157 phenolic moieties (3500 cm^{-1}) can also be noted in the resin spectra and are related to the
158 CN154 oligomer. The spectrum of mimosa tannin powder highlights the characteristic bands
159 of condensed tannin with a broad band at 3250 cm^{-1} assigned to -OH stretching in phenolic
160 structures; multiple signals related to aromatic vibrations (mainly C=C stretching at 1605 and
161 1510 cm^{-1}) and a strong band around 1020 cm^{-1} attributed to C-O stretching of methoxy
162 groups (Tondi and Petutschnigg, 2015). Meanwhile, in the spectrum of the nanocomposite,
163 the characteristics of both acrylate matrix and tannin powder remain discernible and the
164 characteristics bands useful for monitoring the polymerization barely overlap.

165 The photopolymerization reactivities of the resins in ambient air were evaluated by
166 monitoring the C=C band of the acrylate moieties (at 1635 cm^{-1} as seen by FTIR) after
167 different irradiation times. The acrylate resin showed a C=C conversion of over 55% after 3s
168 of irradiation (Figure 2a), and the addition of tannin filler in the photoreactive acrylate resin
169 led to the reduction of the polymerization rate (Figure 2b). Acrylate conversion results
170 measured at 1635 cm^{-1} agree with conversions obtained by monitoring the acrylate C=C band
171 at 810 cm^{-1} . The materials require a longer irradiation time (up to 200 s in the UV oven) to
172 reach their critical conversion/gel point, which remained unchanged compared to the unfilled
173 resin (about 57%). The increase in curing time can be attributed not only to the UV-absorbing
174 moieties of the flavonoids (mostly the aromatic rings) but also to the reddening of the mimosa
175 tannin (Roux et al., 1975). This phenomenon results from the absorption of a photon and
176 subsequent quenching of radical species by oxidation of phenols to quinones, thus hindering

177 free radical polymerization. This phenomenon was observed during FTIR monitoring with the
 178 attenuation of the -OH deformation at 3250 cm^{-1} and, at the same time, in the increase of C=O
 179 vibrations (1720 cm^{-1} peak) for the resin containing tannin after 300 s of light exposure, while
 180 no significant changes were observed for the neat acrylate resin (Figure 2c and d).

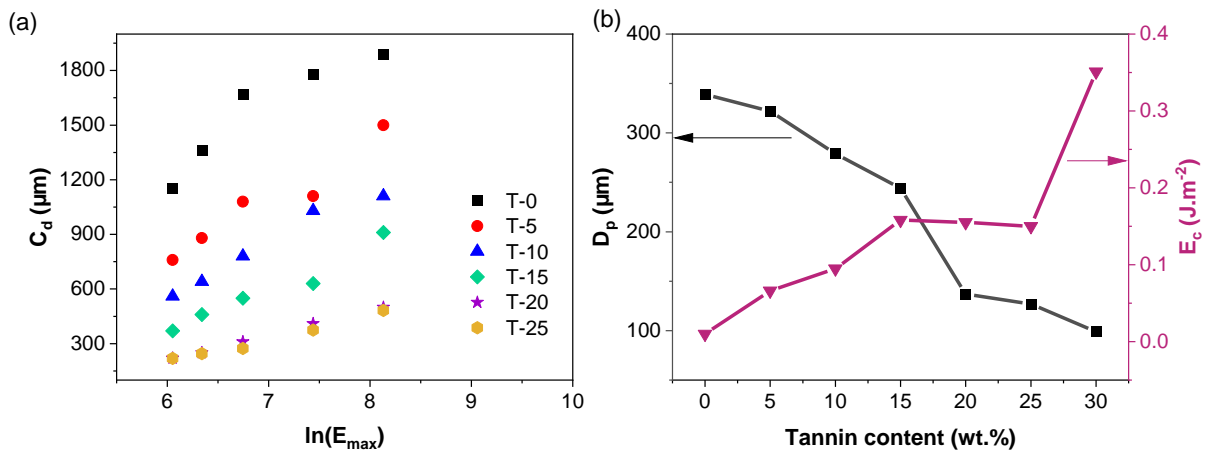


181
 182 **Figure 2.** (a) C=C bond conversion, α , and (b) polymerization rate of the tannin-based resins
 183 as a function of time with a zoom of the boxed area of the graph; FTIR monitoring of (c) -OH
 184 bond stretching (3250 cm^{-1}) and (d) C=O bond stretching (1720 cm^{-1}) of T-0 acrylate resin,
 185 and T-15 acrylate-tannin nanocomposite.

186 3.2. Printing performance

187 The working curve is a semi-empirical model used to formulate photocurable resins
 188 designed for SLA. It provides the threshold energy required to initiate polymerization (E_c ,
 189 $\text{mJ}\cdot\text{cm}^{-2}$) and helps to evaluate printing parameters (such as maximum slice thickness at a
 190 given laser speed, related to D_p), allowing favorable control of resolution and uniformity of
 191 geometry. A resin surface bounded by a 5 mm square was cured in the resin tank using
 192 different laser speeds, *i.e.*, different maximum exposures determined from equation (3).

193 The values of critical energy (E_c) and the depth of penetration (D_p) are presented in Table
 194 S2 and were estimated by regression of the curing depth (C_d) against the natural logarithm of
 195 E_{max} . The plots of the working curve model and results are shown in Figure 3.



196

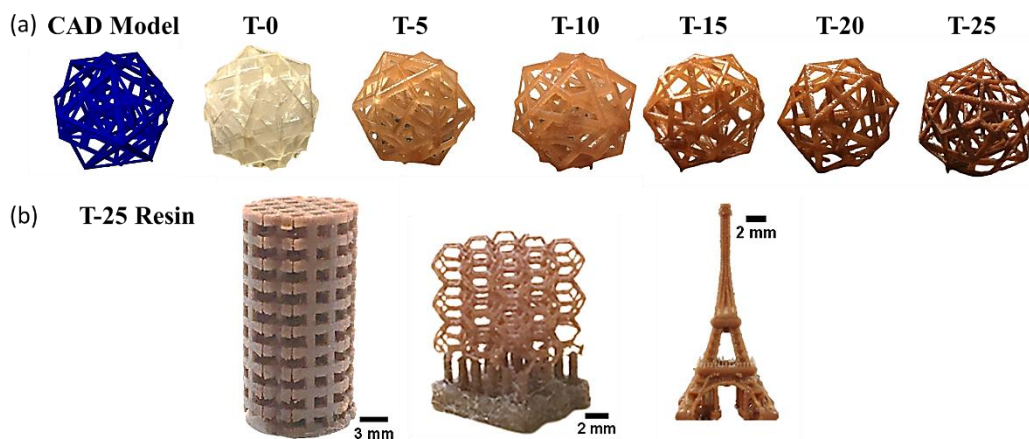
197 **Figure 3.** (a) Working curves showing the curing depth (C_d) as a function of the natural
 198 logarithm of the maximal exposure for the different acrylate-tannin resin formulations; (b)
 199 Curing depth (D_p) and critical energy (E_c) versus tannin content.

200 As expected, the curing depth decreased with the addition of mimosa tannin, with values
 201 ranging from 339 μm to 127 μm . The critical exposure (E_c) determined for the neat acrylate
 202 formulation, with a relatively low value of 17 $\text{mJ}\cdot\text{cm}^{-2}$, is comparable to that of previously
 203 reported resins (Bassett et al., 2020; Sutton et al., 2018; Zhu et al., 2022). E_c increases
 204 significantly with tannin content, with values of 67 and 151 $\text{mJ}\cdot\text{cm}^{-2}$ for T-5 and T-25 resins,

205 respectively. These results are in agreement with the kinetic observations. It is important to
206 note that the formulated resin does not contain commercial photoblockers commonly used to
207 control the resolution by reducing D_p . Thus, the working curves measurements confirmed that
208 tannin also limits the penetration of light through the resin, thus preventing any unintentional
209 polymerization of additional surfaces, and that tannin can therefore be considered a
210 photoinhibitor.

211 3.3. 3D printing of acrylate-tannin composites

212 From the working curves, the laser speed and printing slice thickness could be optimized
213 for all formulations. Figure 4 shows a CAD model of a complex cellular structure, which has
214 been printed using the different tannin based resins. The layer thickness was set to 30 μm .



215

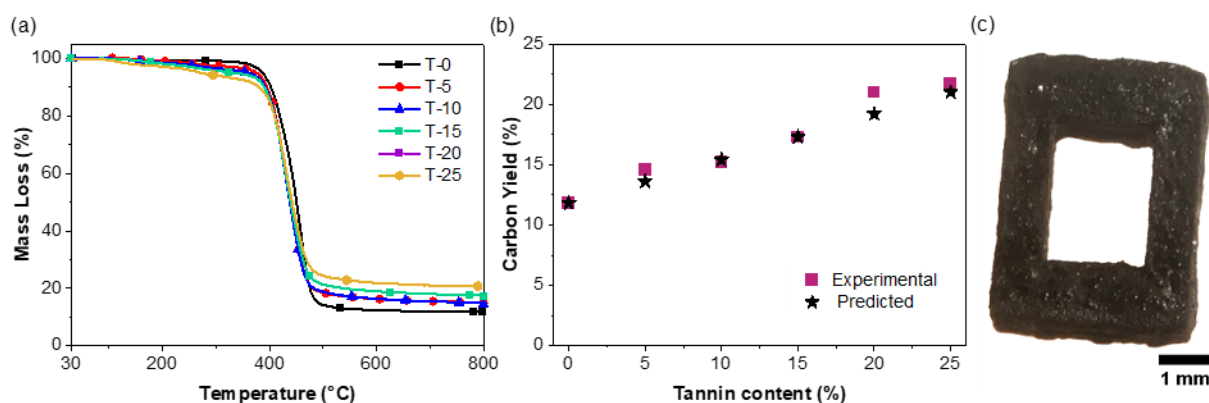
216 **Figure 4.** (a) Digital model of a complex structure (far left of figure), and photographs of
217 the corresponding 3D-printed composites containing 0, 5, 10, 15, 20 and 25 wt.% tannin; (b)
218 Photographs of various 3D-printed architectures obtained with T-25 resin.

219 As can be seen in Figure 4a, the addition of tannin filler to the resin led to a more or less
220 intense reddish-brown coloration. Structures printed with resins containing at least 15 wt.%
221 tannin showed remarkable resolution contrasting with structures based on resins containing
222 few tannin particles and in particular the T-0 based structure, displaying larger strands in spite

223 of using the same laser speed. The excellent resolution of the T-25 resin could be illustrated
224 by several complex structures, such as the Eiffel Tower or Kelvin cells (Figure 4b).

225 *3.4. Thermal behavior*

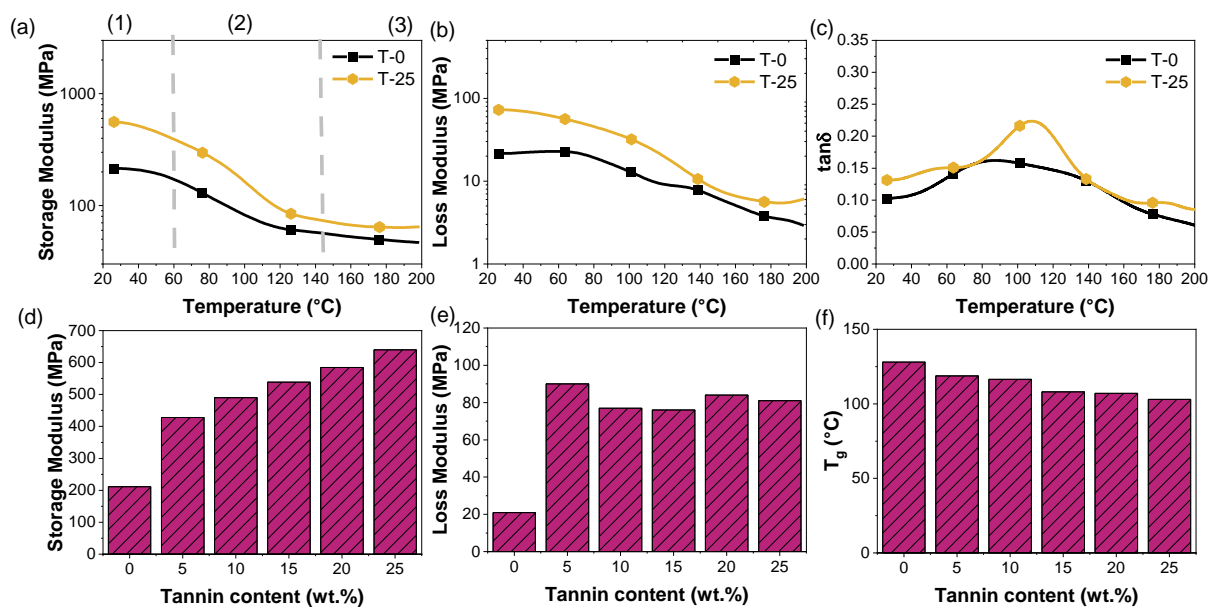
226 Although the SLA technique has the advantage of operating at low temperatures (from
227 room temperature to 35 °C), it is fundamental to study the thermal stability of the composite
228 at high temperature in the context of its possible applications. It is, likewise, necessary to
229 establish the influence of the bio-based filler on this stability. TGA experiments were thus
230 performed to evaluate the influence of mimosa tannin fillers on the thermal properties of the
231 cured acrylate composite. Thermograms of the different 3D-printed specimens, shown in
232 **Figure 5a**, demonstrated good thermal stability up to 170 °C, a temperature at which the
233 acrylate oligomers start to depolymerize, leading to a loss of the lateral and terminal vinyl
234 chain units. The main degradation step, between 300 °C and 680 °C, accounts for a significant
235 weight loss of about 80% and is associated with the carbonization of the polymeric structures.
236 While the thermal degradation events for both neat and composite resin were nearly similar,
237 the former exhibited more significant weight loss at higher temperatures than the latter; tannin
238 is indeed known to have a significant carbon yield close to 45% (Celzard and Fierro, 2020).
239 Although the acrylate-tannin resin displayed slightly lower thermal stability, with a thermal
240 degradation starting a bit earlier than the neat acrylate resin, the addition of the bio-based
241 component led to an increase in carbon yield (**Figure 5b**). The experimental values obtained
242 by TGA are in agreement with the expected carbon yield, calculated as the weighted average
243 of the pyrolysis yields of the acrylate resin on the one hand and the tannins on the other hand.
244 These results suggest the possibility of printing high-yield carbon structures (an example of
245 which is presented in **Figure 5c**) in a reduced number of steps with the precision of SLA
246 (Blyweert et al., 2022b, 2022a).



247
 248 **Figure 5.** (a) Weight loss of cured acrylate and tannin-based materials; (b) Carbon yield
 249 versus tannin content; and (c) an example of 3D-printed carbon architecture derived from
 250 acrylate-tannin composite.

251 *3.5. Thermomechanical properties*

252 The viscoelastic behaviors of the printed composites with different tannin content were
 253 characterized by DTMA, and the corresponding data are summarized in Table S3.



254
 255 **Figure 6.** (a) Storage modulus, (b) Loss modulus and (c) Loss angle tangent, $\tan\delta$ as a
 256 function of temperature; (d) Storage modulus at 25 °C; (e) Loss modulus at 25 °C; and (f)
 257 Glass transition temperature as function of tannin content.

258 The plots of storage modulus versus temperature for the nanocomposites and the neat
259 acrylate polymer are shown in Figure 6a and Figure S1a. Between 20 °C and 200 °C, three
260 main zones were revealed: (1) the glassy region, (2) the transition region, and (3) the rubbery
261 plateau. In the glassy region, the bio-based composites exhibit typical highly crosslinked
262 thermoset behavior with relatively high storage modulus (E') values. At 25 °C, E' increased
263 from 211.1 MPa for the pristine resin to 639.9 MPa with the addition of 25 wt.% tannin. The
264 mechanical improvement can be attributed to the stiffness of the tannin particles. In addition,
265 the storage modulus decreased with temperature to reach the rubbery plateau. As the
266 nanocomposites started to degrade around 170 °C, no cold crystallization zone was observed.

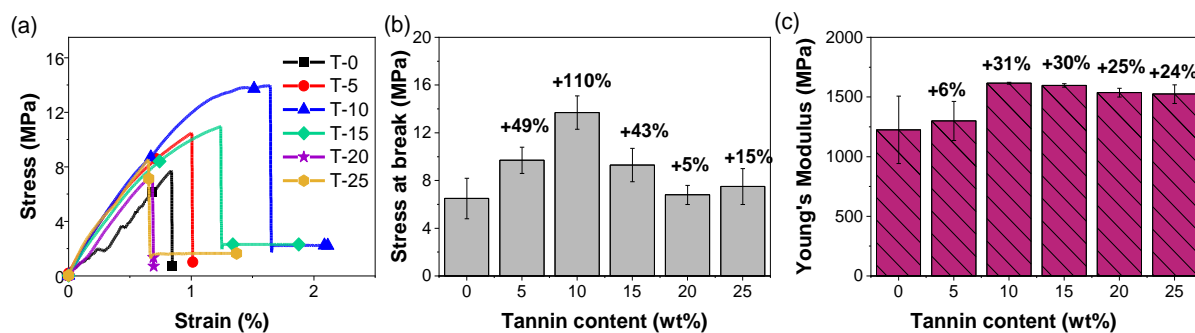
267 The viscous response of the composites described by the loss modulus (E'') is represented
268 in Figure 6b and Figure S1b. As expected, due to a greater free movement of the polymer
269 chains, E'' decreased with temperature. Moreover, with the increase in internal friction
270 between the matrix polymer chains and the tannin particle, a positive shift of the maximum
271 loss modulus peak to higher temperatures for the acrylate-tannin composites was observed.

272 The glass transition temperature (T_g) values, obtained from the maximum of $\tan \delta$
273 (ISO/ASTM, 2012; Maalihan et al., 2022) in Figure 6c and Figure S1c, decreased from
274 128 °C for the neat acrylate resin to 103 °C for the T-25 composite. These results are
275 consistent with a previous study using the same printed material but with T_g measurements
276 performed by DSC analysis (Blyweert et al., 2022b). The shift in T_g to lower temperatures
277 suggests an increase in interfacial interactions and a change in apparent relaxation time
278 resulting from the addition of stiff microparticles (Bashir, 2021; Wood et al., 2016).

279 *3.6. Mechanical properties at room temperature*

280 Tensile tests at room temperature were performed to determine the effect of tannin on the
281 properties of acrylate and composite resins in their glassy state. Figure 7 shows representative

282 stress-strain curves for the different tannin contents and the evolution of Young's modulus
 283 and stress at break with tannin content. The neat acrylate resin has a tensile strength of 6.5
 284 MPa, which improves by 110% upon the addition of 10 wt.% tannin powder (13.7 MPa)
 285 while decreasing to 9.3, 6.8 and 7.4 MPa with the addition of 15, 20 and 25 wt.% tannin,
 286 respectively (see Table S4 and Figure 7b). The Young's modulus of the pristine acrylate resin
 287 (1225.3 MPa) was also significantly increased by the addition of 10 wt.% tannin. Unlike the
 288 tensile strength, only a slight decrease is observed with the addition of more tannin particles
 289 (Figure 7c).



290
 291 **Figure 7.** (a) Stress-strain curves; (b) Tensile strength and (c) Young's modulus of cured
 292 acrylate and tannin-based materials.

293 Overall, the tensile strength and Young's modulus of acrylate-tannin composites were
 294 improved compared to the neat acrylate polymer, which is important enough to be highlighted.
 295 In fact, due to the reduced interaction between the matrix and the filler, limited reinforcement
 296 at high loading is commonly observed in biomass-derived resins for SLA (Zhang et al., 2021).
 297 It was also observed that the elongation at break (*i.e.*, ductility) increased from 0.8 to 1.4 %
 298 with the addition of 10 wt.% tannin particles and decreased slightly to 0.85 % for T-20 and T-
 299 25 resins. Although the structure remains brittle, the addition of tannin demonstrated the
 300 ability to deform plastically with the matrix without debonding, leading to improved ductility
 301 compared to that measured on the neat formulated polymer. Therefore, the mechanical
 302 properties of 3D acrylate-tannin composites are comparable to those obtained using wood- or

303 lignin-based resins for SLA, as shown in Table 1 (Sutton et al., 2021, 2018; Yao and
304 Hakkarainen, 2023; Zhang et al., 2021)

305 **Table 1.** Mechanical performances of the materials in this study and other bio-based SLA-
306 printed composites reported in the literature.

Tensile strength (MPa)	Young's modulus (MPa)	Ref.
13.7	1616	This work – 10 wt.% tannin (Yao and Hakkarainen, 2023) –
3.0	71	10 wt.% of microwave- methacrylated wood flour (Zhang et al., 2021) – 10 wt.% of
9	100	wood flour (Sutton et al., 2021) – 10 wt.% of
18	480	acylated lignin

307

308 **4. Conclusion**

309 Greener and more mechanically robust 3D-printed structures are obtained when adding
310 tannin concentrations (5 to 25 wt.%) to an acrylate resin. Acrylate-tannin resins were prepared
311 via a simple mixing technique and printed using a desktop stereolithography 3D printer. The
312 formulated photocurable acrylate resins showed attractive acrylate C=C bond conversion
313 above 55%. Although the addition of tannin reduced the polymerization rate, because tannin
314 also acts as a UV photoblocker in the resin, it did not affect the final conversion.

315 The acrylate-tannin composites evidenced high storage modulus, from 200 to 690 MPa at
316 25 °C, and enhanced mechanical properties in their glassy state. Indeed, a maximal increase
317 by 110%, 80%, and 32% was observed for strength, ductility, and modulus, respectively, with
318 the addition of 10 wt.% filler. At higher tannin content, the mechanical properties remained

319 superior to those observed for the pristine resin. Overall, with adequate viscosity at 100 s^{-1}
320 shear, moderate curing energy combined with attractive printing performances and
321 mechanical properties, tannin-based resins have the potential to be used as a component in the
322 development of bio-based materials for laser stereolithography.

323 **CRedit authorship contribution statement**

324 **Pauline Blyweert:** Conceptualization, Investigation, Writing – original draft, Writing –
325 Review & Editing. **Vincent Nicolas:** Supervision, Writing- Review & Editing. **Vanessa**
326 **Fierro:** Funding acquisition, Supervision, Writing - Review & Editing. **Alain Celzard:**
327 Conceptualization, Supervision, Funding acquisition, Writing - Review & Editing.

328 **Declaration of competing interest**

329 The authors declare no conflict of interest for this work.

330 **Acknowledgements**

331 We are very grateful to Sartomer France (Arkema Group) for providing the monomers
332 used in this work, to Sébastien Schaeffer for the DTMA tutorials and to Philippe Gadonneix
333 for the technical support.

334 PB thanks the financial support of the Grand-Est region and the French Ministry of Higher
335 Education for her PhD grant.

336 **Funding sources**

337 The project was partially funded by ERDF [TALiSMAN project (2019-000214)] and was
338 also sponsored by the NATO Science for Peace and Security Program [Grant G5697
339 CERTAIN “Globular carbon-based structures and metamaterials for enhanced
340 electromagnetic protection”].

- 342 Ambrogi, V., Cerruti, P., Carfagna, C., Malinconico, M., Marturano, V., Perrotti, M., Persico,
343 P., 2011. Natural antioxidants for polypropylene stabilization. *Polymer Degradation*
344 *and Stability* 96, 2152–2158. <https://doi.org/10.1016/j.polymdegradstab.2011.09.015>
- 345 Anastasio, R., Peerbooms, W., Cardinaels, R., van Breemen, L.C.A., 2019. Characterization
346 of Ultraviolet-Cured Methacrylate Networks: From Photopolymerization to Ultimate
347 Mechanical Properties. *Macromolecules* 52, 9220–9231.
348 <https://doi.org/10.1021/acs.macromol.9b01439>
- 349 Anwer, M.A.S., Naguib, H.E., Celzard, A., Fierro, V., 2015. Comparison of the thermal,
350 dynamic mechanical and morphological properties of PLA-Lignin & PLA-Tannin
351 particulate green composites. *Composites Part B: Engineering* 82, 92–99.
352 <https://doi.org/10.1016/j.compositesb.2015.08.028>
- 353 Bashir, M.A., 2021. Use of Dynamic Mechanical Analysis (DMA) for Characterizing
354 Interfacial Interactions in Filled Polymers. *Solids* 2, 108–120.
355 <https://doi.org/10.3390/solids2010006>
- 356 Bassett, A.W., Honnig, A.E., Breyta, C.M., Dunn, I.C., La Scala, J.J., Stanzione, J.F., 2020.
357 Vanillin-Based Resin for Additive Manufacturing. *ACS Sustainable Chem. Eng.* 8,
358 5626–5635. <https://doi.org/10.1021/acssuschemeng.0c00159>
- 359 Blyweert, P., Nicolas, V., Fierro, V., Celzard, A., 2023. 3D-Printed Carbons with Improved
360 Properties and Oxidation Resistance. *ACS Sustainable Chem. Eng.*
361 <https://doi.org/10.1021/acssuschemeng.3c00152>
- 362 Blyweert, P., Nicolas, V., Fierro, V., Celzard, A., 2022a. Experimental design optimisation of
363 tannin-acrylate photocurable resins for 3D printing of biobased porous carbon
364 architectures. *Molecules*. <https://doi.org/10.3390/molecules27072091>
- 365 Blyweert, P., Nicolas, V., Fierro, V., Celzard, A., 2021. 3D printing of carbon-based
366 materials : a review. *Carbon* 183, 449–485.
367 <https://doi.org/10.1016/j.carbon.2021.07.036>
- 368 Blyweert, P., Nicolas, V., Macutkevic, J., Fierro, V., Celzard, A., 2022b. Tannin-based resins
369 for 3D printing of porous carbon architectures. *ACS Sustainable Chem. Eng.*
370 <https://doi.org/10.1021/acssuschemeng.2c01686>
- 371 Braghiroli, F.L., Amaral-Labat, G., Boss, A.F.N., Lacoste, C., Pizzi, A., 2019. Tannin Gels
372 and Their Carbon Derivatives: A Review. *Biomolecules* 9, 587.
373 <https://doi.org/10.3390/biom9100587>
- 374 Celzard, A., Fierro, V., 2020. “Green”, innovative, versatile and efficient carbon materials
375 from polyphenolic plant extracts. *Carbon* 167, 792–815.
376 <https://doi.org/10.1016/j.carbon.2020.05.053>
- 377 Cingesar, I.K., Marković, M.-P., Vrsaljko, D., 2022. Effect of post-processing conditions on
378 polyacrylate materials used in stereolithography. *Additive Manufacturing* 55, 102813.
379 <https://doi.org/10.1016/j.addma.2022.102813>
- 380 Feng, X., Yang, Z., Wang, S., Wu, Z., 2022. The reinforcing effect of lignin-containing
381 cellulose nanofibrils in the methacrylate composites produced by stereolithography.
382 *Polymer Engineering & Science* 62, 2968–2976. <https://doi.org/10.1002/pen.26077>
- 383 ISO/ASTM, 2016. Terminology for Additive Manufacturing - General Principles -
384 Terminology. ASTM International. <https://doi.org/10.1520/ISOASTM52900-15>
- 385 ISO/ASTM, 2012. Plastics — Determination of tensile properties — Part 2: Test conditions
386 for moulding and extrusion plastics - ISO 527-2. ASTM International.
- 387 Jacobs, P.F., 1992. Fundamentals of Stereolithography. International Solid Freeform
388 Fabrication Symposium.

389 Kumar, S., Hofmann, M., Steinmann, B., Foster, E.J., Weder, C., 2012. Reinforcement of
390 Stereolithographic Resins for Rapid Prototyping with Cellulose Nanocrystals. *ACS*
391 *Appl. Mater. Interfaces* 4, 5399–5407. <https://doi.org/10.1021/am301321v>
392 Lee, J.H., Prud'homme, R.K., Aksay, I.A., 2001. Cure depth in photopolymerization:
393 Experiments and theory. *J. Mater. Res.* 16, 3536–3544.
394 <https://doi.org/10.1557/JMR.2001.0485>
395 Lee, T.Y., Roper, T.M., Jonsson, E.S., Kudyakov, I., Viswanathan, K., Nason, C., Guymon,
396 C.A., Hoyle, C.E., 2003. The kinetics of vinyl acrylate photopolymerization. *Polymer*
397 44, 2859–2865. [https://doi.org/10.1016/S0032-3861\(03\)00213-1](https://doi.org/10.1016/S0032-3861(03)00213-1)
398 Liao, J., Brosse, N., Pizzi, A., Hoppe, S., Zhou, X., Du, G., 2020. Characterization and 3D
399 printability of poly (lactic acid)/acetylated tannin composites. *Industrial Crops and*
400 *Products* 149, 112320. <https://doi.org/10.1016/j.indcrop.2020.112320>
401 Lobry, L., Lemaire, E., Blanc, F., Gallier, S., Peters, F., 2019. Shear thinning in non-
402 Brownian suspensions explained by variable friction between particles. *Journal of*
403 *Fluid Mechanics* 682–710. <https://doi.org/10.1017/jfm.2018.881>
404 Maalihan, R.D., Chen, Q., Tamura, H., Sta. Agueda, J.R.H., Pajarito, B.B., Caldon, E.B.,
405 Advincula, R.C., 2022. Mechanically and Thermally Enhanced 3D-Printed
406 Photocurable Polymer Nanocomposites Containing Functionalized Chitin
407 Nanowhiskers by Stereolithography. *ACS Appl. Polym. Mater.* 4, 2513–2526.
408 <https://doi.org/10.1021/acsapm.1c01816>
409 Maalihan, R.D., Pajarito, B.B., Advincula, R.C., 2020. 3D-printing methacrylate/chitin
410 nanowhiskers composites via stereolithography: Mechanical and thermal properties.
411 *Materials Today: Proceedings*, 10th International Conference on Key Engineering
412 *Materials* 2020 33, 1819–1824. <https://doi.org/10.1016/j.matpr.2020.05.063>
413 Manapat, J.Z., Chen, Q., Ye, P., Advincula, R.C., 2017a. 3D Printing of Polymer
414 Nanocomposites via Stereolithography. *Macromol. Mater. Eng.* 302, 1600553.
415 <https://doi.org/10.1002/mame.201600553>
416 Manapat, J.Z., Mangadlao, J.D., Tiu, B.D.B., Tritchler, G.C., Advincula, R.C., 2017b. High-
417 Strength Stereolithographic 3D Printed Nanocomposites: Graphene Oxide
418 Metastability. *ACS Appl. Mater. Interfaces* 9, 10085–10093.
419 <https://doi.org/10.1021/acsami.6b16174>
420 Mangesana, N., Mainza, A., Govender, I., Van der Westhuizen, A., Narasimha, M., 2008. The
421 effect of particle sizes and solids concentration on the rheology of silica sand based
422 suspensions. *Journal of the Southern African Institute of Mining and Metallurgy* 108.
423 McAninch, I.M., Palmese, G.R., Lenhart, J.L., La Scala, J.J., 2015. DMA testing of epoxy
424 resins: The importance of dimensions. *Polymer Engineering & Science* 55, 2761–2774.
425 <https://doi.org/10.1002/pen.24167>
426 Mewis, J., 1980. Rheology of Suspensions, in: Astarita, G., Marrucci, G., Nicolais, L. (Eds.),
427 *Rheology*. Springer US, Boston, MA, pp. 149–168. https://doi.org/10.1007/978-1-4684-3740-9_10
428
429 Oliaei, S.N.B., Behzad, N., 2019. 6. Stereolithography and its applications, in: Davim, J.P.
430 (Ed.), *Additive and Subtractive Manufacturing*. De Gruyter, pp. 229–250.
431 <https://doi.org/10.1515/9783110549775-006>
432 Pagac, M., Hajnys, J., Ma, Q.-P., Jancar, L., Jansa, J., Stefek, P., Mesicek, J., 2021. A Review
433 of Vat Photopolymerization Technology: Materials, Applications, Challenges, and
434 Future Trends of 3D Printing. *Polymers* 13, 598.
435 <https://doi.org/10.3390/polym13040598>
436 Palaganas, J.O., Palaganas, N.B., Ramos, L.J.I., David, C.P.C., 2019. 3D Printing of Covalent
437 Functionalized Graphene Oxide Nanocomposite via Stereolithography. *ACS Appl.*
438 *Mater. Interfaces* 11, 46034–46043. <https://doi.org/10.1021/acsami.9b12071>

439 Quan, H., Zhang, T., Xu, H., Luo, S., Nie, J., Zhu, X., 2020. Photo-curing 3D printing
440 technique and its challenges. *Bioactive Materials* 5, 110–115.
441 <https://doi.org/10.1016/j.bioactmat.2019.12.003>

442 Romero-Ocaña, I., Delgado, N.F., Molina, S.I., 2022. Biomass waste from rice and wheat
443 straw for developing composites by stereolithography additive manufacturing.
444 *Industrial Crops and Products* 189, 115832.
445 <https://doi.org/10.1016/j.indcrop.2022.115832>

446 Roux, D.G., Ferreira, D., Hundt, H. K., Malan, E., 1975. Structure, stereochemistry, and
447 reactivity of natural condensed tannins as basis for their extended industrial
448 application. *Appl. Polym. Symp.* 28, 335–353.

449 Sutton, J.T., Rajan, K., Harper, D.P., Chmely, S.C., 2021. Improving UV Curing in
450 Organosolv Lignin-Containing Photopolymers for Stereolithography by Reduction
451 and Acylation. *Polymers* 13, 3473. <https://doi.org/10.3390/polym13203473>

452 Sutton, J.T., Rajan, K., Harper, D.P., Chmely, S.C., 2018. Lignin-Containing Photoactive
453 Resins for 3D Printing by Stereolithography. *ACS Appl. Mater. Interfaces* 10, 36456–
454 36463. <https://doi.org/10.1021/acsami.8b13031>

455 Tan, H.W., Choong, Y.Y.C., Kuo, C.N., Low, H.Y., Chua, C.K., 2022. 3D printed electronics:
456 Processes, materials and future trends. *Progress in Materials Science* 127, 100945.
457 <https://doi.org/10.1016/j.pmatsci.2022.100945>

458 Thakar, C.M., Parkhe, S.S., Jain, A., Phasinam, K., Murugesan, G., Ventayen, R.J.M., 2022.
459 3d Printing: Basic principles and applications. *Materials Today: Proceedings*,
460 CMAE'21 51, 842–849. <https://doi.org/10.1016/j.matpr.2021.06.272>

461 Tondi, G., Petutschnigg, A., 2015. Middle infrared (ATR FT-MIR) characterization of
462 industrial tannin extracts. *Industrial Crops and Products* 65, 422–428.
463 <https://doi.org/10.1016/j.indcrop.2014.11.005>

464 V. Dhawale, P., K. Vineeth, S., V. Gadhve, R., J, J.F.M., Vijay Supekar, M., Kumar Thakur,
465 V., Raghavan, P., 2022. Tannin as a renewable raw material for adhesive applications:
466 a review. *Materials Advances* 3, 3365–3388. <https://doi.org/10.1039/D1MA00841B>

467 Weng, Z., Zhou, Y., Lin, W., Senthil, T., Wu, L., 2016. Structure-property relationship of
468 nano enhanced stereolithography resin for desktop SLA 3D printer. *Composites Part A:
469 Applied Science and Manufacturing* 88, 234–242.
470 <https://doi.org/10.1016/j.compositesa.2016.05.035>

471 Wood, C.D., Ajdari, A., Burkhart, C.W., Putz, K.W., Brinson, L.C., 2016. Understanding
472 competing mechanisms for glass transition changes in filled elastomers. *Composites
473 Science and Technology* 127, 88–94.
474 <https://doi.org/10.1016/j.compscitech.2016.02.027>

475 Wu, H., Fahy, W.P., Kim, S., Kim, H., Zhao, N., Pilato, L., Kafi, A., Bateman, S., Koo, J.H.,
476 2020. Recent developments in polymers/polymer nanocomposites for additive
477 manufacturing. *Progress in Materials Science* 111, 100638.
478 <https://doi.org/10.1016/j.pmatsci.2020.100638>

479 Yao, J., Hakkarainen, M., 2023. Methacrylated wood flour-reinforced “all-wood” derived
480 resin for digital light processing (DLP) 3D printing. *Composites Communications* 38,
481 101506. <https://doi.org/10.1016/j.coco.2023.101506>

482 Zakeri, S., Vippola, M., Levänen, E., 2020. A comprehensive review of the
483 photopolymerization of ceramic resins used in stereolithography. *Additive
484 Manufacturing* 35, 101177. <https://doi.org/10.1016/j.addma.2020.101177>

485 Zhang, J., Hu, Q., Wang, S., Tao, J., Gou, M., 2020. Digital Light Processing Based Three-
486 dimensional Printing for Medical Applications. *International Journal of Bioprinting* 6.
487 <https://doi.org/10.18063/ijb.v6i1.242>

- 488 Zhang, S., Bhagia, S., Li, M., Meng, X., Ragauskas, A.J., 2021. Wood-reinforced composites
489 by stereolithography with the stress whitening behavior. *Materials & Design* 206,
490 109773. <https://doi.org/10.1016/j.matdes.2021.109773>
- 491 Zhang, S., Li, M., Hao, N., Ragauskas, A.J., 2019. Stereolithography 3D Printing of Lignin-
492 Reinforced Composites with Enhanced Mechanical Properties. *ACS Omega* 4, 20197–
493 20204. <https://doi.org/10.1021/acsomega.9b02455>
- 494 Zhang, X., Xu, Y., Li, L., Yan, B., Bao, J., Zhang, A., 2019. Acrylate-based photosensitive
495 resin for stereolithographic three-dimensional printing. *Journal of Applied Polymer
496 Science* 136, 47487. <https://doi.org/10.1002/app.47487>
- 497 Zhao, J., Yang, Y., Li, L., 2020. A comprehensive evaluation for different post-curing
498 methods used in stereolithography additive manufacturing. *Journal of Manufacturing
499 Processes* 56, 867–877. <https://doi.org/10.1016/j.jmapro.2020.04.077>
- 500 Zhu, G., Zhang, J., Huang, J., Yu, X., Cheng, J., Shang, Q., Hu, Y., Liu, C., Zhang, M., Hu, L.,
501 Zhou, Y., 2022. Self-Healing, Antibacterial, and 3D-Printable Polymerizable Deep
502 Eutectic Solvents Derived from Tannic Acid. *ACS Sustainable Chem. Eng.* 10, 7954–
503 7964. <https://doi.org/10.1021/acssuschemeng.2c01328>
504